

Dalton Transactions

Accepted Manuscript



This is an *Accepted Manuscript*, which has been through the Royal Society of Chemistry peer review process and has been accepted for publication.

Accepted Manuscripts are published online shortly after acceptance, before technical editing, formatting and proof reading. Using this free service, authors can make their results available to the community, in citable form, before we publish the edited article. We will replace this *Accepted Manuscript* with the edited and formatted *Advance Article* as soon as it is available.

You can find more information about *Accepted Manuscripts* in the [Information for Authors](#).

Please note that technical editing may introduce minor changes to the text and/or graphics, which may alter content. The journal's standard [Terms & Conditions](#) and the [Ethical guidelines](#) still apply. In no event shall the Royal Society of Chemistry be held responsible for any errors or omissions in this *Accepted Manuscript* or any consequences arising from the use of any information it contains.



Journal Name

ARTICLE

Phase development during high-energy ball-milling of zinc oxide and iron – the impact of grain size on the source and the degree of contamination

Received 00th January 20xx,
Accepted 00th January 20xx

DOI: 10.1039/x0xx00000x

www.rsc.org/

G. Štefanić, S. Krehula and I. Štefanić

High-energy ball-milling of powder mixtures of zincite (ZnO) and iron (α -Fe) at different weight ratios was performed in air using the planetary ball mill with a stainless steel milling assembly. Structural and microstructural changes during the ball-milling (up to 30 h) were monitored using X-ray powder diffraction, field emission scanning electron microscopy (FE SEM) and UV-Vis diffuse reflectance spectroscopy. The mechanism of iron oxidation was determined from the results of Mössbauer spectroscopy. It was found that an early phase of ball-milling caused the oxidation of iron from Fe^0 to Fe^{2+} followed by the formation of a solid solution structurally similar to wüstite. The wüstite-type phase rapidly disappeared upon prolonged milling, which was accompanied by further oxidation of iron from Fe^{2+} to Fe^{3+} and the formation of spinel-type ferrite structurally similar to franklinite (ZnFe_2O_4) in the products with high zinc content, or magnetite (Fe_3O_4) in the products with high iron content. Further milling or annealing had a low impact on the franklinite-type phase, but caused the transition of the magnetite-type phase to the phase structurally similar to hematite (α - Fe_2O_3). The results of energy dispersive X-ray spectrometry (EDS) showed a dramatic increase in the degree of contamination with the increase in the proportion of the starting iron (~9 times higher contamination during the milling of pure iron compared with pure zincite). It was shown that the source of contamination (balls or vial) strongly depends on the type of milled sample. Ball-milling of relatively big and heavy grains (starting iron) caused preferential contamination from the vial whereas ball-milling of smaller and lighter grains (products obtained after prolonged milling) caused preferential contamination from the balls. After prolonged milling the contamination due to wear of the balls was dominant in all the products. An explanation for the observed impact of grain size on the source and the degree of contamination was proposed.

Introduction

In the past ten years the mechanosynthesis of organic and pharmaceutical materials has received growing attention as a solvent-free and low-energy synthetic route.^{1,2} The use of mechanical milling in the preparation of inorganic materials (ceramics, metals, alloys) has a much longer tradition,³⁻⁵ and various aspects of such processing were summarized in several review papers.⁵⁻¹² In contrast to the mechanosynthesis of organic compounds, processing of inorganic materials is generally more energy demanding and often requires highly energetic milling for an extended length of time. Contamination of milled sample due to the attrition of milling assembly (balls and vial) is a major obstacle during the high energy ball-milling. There are a number of

processing parameters that could/should be optimized in order to obtain the desired products with minimum contamination. Several steps have been proposed in order to reduce the effects of contamination.^{6-9,11} Milling time should be kept as short as possible. If possible, milling media should be made up of the same material as that of the milled powders (due to a limited amount of commercially available materials for a milling assembly this suggestion could rarely be fulfilled). If the use of a milling assembly made of the same material as milled powders is not possible, the milling assembly should be made of a material harder/stronger than the powder being milled. It was shown that the coating of the balls and the vial with milled powders significantly reduced further contamination.^{8,13} However, a systematic investigation of the effect of processing parameters on the amount of contamination has not been undertaken yet. Some important milling parameters are: the type of mill (most serious contamination from highly energetic mills, e.g., SPEX shaker mill), milling container, milling speed, milling time, type and size of the milling medium, ball-to-powder weight ratio, the extent of filling the vial, milling atmosphere, the presence of a process control agent, temperature of milling, etc. Most of these parameters are interconnected, which significantly complicates the selection of optimum conditions. For example,

Division of Materials Chemistry, Ruđer Bošković Institute, P.O. Box 180,
HR-10002 Zagreb, Croatia. E-mail: stefanic@irb.hr; Fax: +385-1-46-80084;
Tel: +385-1-456-1111 here.

† Electronic supplementary information (ESI) available: Colors of the products;
Quantitative crystal phase analysis (Table 1); Unit-cell Parameter (Table 2);
Mössbauer spectroscopy (Tables 3, 4, 5 and 6); FE-SEM analysis; EDS analysis. See
DOI: 10.1039/x0xx00000x

optimum milling time will depend on almost all other parameters. In practice, most investigators optimize only several milling parameters and often just one (milling duration).⁹

In our previous studies we examined the effect of high-energy ball-milling on the structural and microstructural changes in monoclinic zirconia (ZrO₂).^{14,15} It has been documented for some time that such milling can induce partial stabilization of high-temperature tetragonal and cubic polymorphs of ZrO₂.¹⁶⁻¹⁸ Stabilization of these polymorphs was attributed to the surface energy effect in accordance with the model proposed by Garvie.¹⁹ Our investigation showed that a significant reduction in monoclinic ZrO₂ crystallite size (below 10 nm) caused only a partial stabilization of tetragonal ZrO₂ (up to ~30 vol%) when the corundum or agate milling assembly were used.¹⁵ In case of the zirconia milling assembly a reduction in monoclinic ZrO₂ crystallite size has an even smaller impact on the formation of high-temperature polymorphs.²⁰ However, a complete transition, first to tetragonal and after prolonged milling to cubic ZrO₂ occurred when the steel milling assembly was used.¹⁴ It was shown that Fe³⁺ ions, introduced due to the wear and oxidation of the steel milling assembly, incorporated into the ZrO₂ lattice and stabilized high-temperature polymorphs of ZrO₂ in a way described for the system ZrO₂-Fe₂O₃.^{21,22} Such stabilization could not be obtained with other milling assemblies, regardless of the amount of the introduced impurities (the corundum assembly introduced a significantly higher amount of impurities).¹⁵

Due to the high density and low cost steel is a common type of material used in high-energy milling, and particularly for milling samples that contain iron, such as ferrites. A chemical reaction between iron contamination from the steel milling assembly and milled oxides, clearly demonstrated in the case of zirconia, has been reported in several investigations.²³⁻²⁷ However, the danger posed by the improper use of steel milling tools in high-energy milling is still generally neglected. An overview of the papers connected with the mechanosynthesis of spinel-type ferrites revealed significant discrepancies between the reported milling conditions and steel contamination.²⁸ Most reports neglected the presence of contamination, although the intensity of milling was often greater compared with the intensities of milling in a few papers that have reported the presence of significant contamination.^{24,26,28} The occurrence of iron in a lower oxidation state during the milling of hematite in air is observed and discussed in several studies.^{24,29-43} In a review paper related to this area Šepelák noted that the appearance of reducing iron comes only in cases where grinding is carried out with a tool made of steel, while the use of tools made of corundum or heavier tungsten carbide does not lead to reduction.⁴³

Our recent research shows that the milling atmosphere has a very high impact on the amount of steel contamination and its interaction with milled samples during the standard high-energy ball-milling.²⁸ The rate of contamination significantly increases in the non-oxidative atmosphere (nitrogen) due to the abrasion of milling tools by steel chips coming from it. The self-propagation of this process causes an increased rate of contamination with the

prolonged milling time that could not be prevented by coating the milling tools with milled powder. The rate of contamination during the high-energy milling in the oxidative atmosphere (air) is slower because steel particles introduced due to the abrasion of milling tools quickly oxidize and disappear. However, the obtained iron ions (Fe²⁺ and Fe³⁺) easily incorporate into the structure of milled sample and cause structural changes (formation of zinc ferrite from zincite). The mechanism of iron oxidation during this process remains unclear due to the continuous entering and oxidation of freshly formed steel chips.²⁸

The aim of the present investigation was to determine the mechanism of iron oxidation during high-energy ball-milling in air and the impact of samples abrading capacity on the rate and mechanism of contamination from the milling assembly. In this study we used standard milling conditions that can often be found in literature related to the mechanosynthesis of ferrites.²⁸ In order to get a better insight into the mechanism of iron oxidation we examined the products of high-energy milling of zincite (ZnO) and iron (α -Fe) powder mixtures at different weight ratios.

Experimental

Chemicals and Synthesis

The starting chemicals were ultra-pure zincite (ZnO, space group *P6₃mc*, *a* = 3.24982 Å, *c* = 5.20661 Å; ICDD PDF No. 36-1451) powder (*Ventron*) and iron (α -Fe, space group *Im $\bar{3}m$* , *a* = 2.8664 Å; ICDD PDF No. 6-696) powder, -200 mesh, >99% metals basis (*Alfa Aesar*). High-energy ball-milling of pure zincite powder (sample S1), the powder mixtures of zincite and iron with weight ratios of 3:1 (sample S2), 1:1 (sample S3) and 1:3 (sample S4) and pure iron powder (sample S5) was performed in air using the *Fritsch* planetary ball mill *Pulverisette 6*. In the milling we used ten stainless steel balls (ball diameter = 10 mm) and steel bowl of 80 cm³. The results of EDS analysis indicate that the stainless steel balls contain ~84% of Fe, ~15% of Cr and ~1% of other elements (Si, Mn), while the stainless steel grinding bowl contain ~71% of Fe, ~21% of Cr, ~6% of Ni and some traces of other elements (Si, Mn). The main disk rotation speed was 500 rpm and the powder-to-ball weight ratio 1:20. The milling time varied from 1 to 30 hours. A small amount of samples (~50 mg, ~2.5% of starting samples mass) was taken at selected times for analysis. After each hour of milling the bowl was left with open lid to cool down for 5 minutes. The obtained milling products were notated with the name of starting sample (S1 to S5) and number (1 to 30), standing for the milling time in hours. For the thermal stability study, the products obtained after 30 h of ball-milling (samples S1-30, S2-30, S3-30, S4-30 and S5-30) were subjected to temperature treatment at 500 °C and 1000 °C for 2 h.

Instruments and Characterization

Structural and microstructural changes in the ball-milled products were investigated at room temperature (RT) using X-ray powder

diffraction (XRD), ^{57}Fe Mössbauer spectroscopy, field emission scanning electron microscopy (FE SEM), energy dispersive X-ray spectrometry (EDS) and UV-Vis-NIR spectroscopy. The obtained results are presented graphically while the corresponding numerical values are shown in ESI (Tables 1 to 6 and Figs. 19 to 61).

XRD measurements were taken in step-scan mode using an *ItalStructures* diffractometer APD2000 with monochromatized $\text{CuK}\alpha$ radiation (graphite monochromator). Rietveld refinements⁴⁴ (program MAUD⁴⁵) of powder diffraction patterns were used for a quantitative crystal phase analysis of ball-milled products (Fig. 3a and Table 1 in ESI). Precise lattice parameters of the spinel ferrite phase obtained in the products of ball-milling was determined from the results of Le Bail refinements⁴⁶ of powder diffraction patterns (program GSAS⁴⁷ with a graphical user interface EXPGUI⁴⁸). Silicon (*Koch-Light Lab. Ltd.*) was used as an internal standard (space group $Fd\bar{3}m$; $a = 5.43088 \text{ \AA}$; JCPDS-ICDD PDF card No. 27-1402). The physical broadening (β) of the most prominent diffraction lines of zincite and α -iron was used to estimate the volume-averaged domain size (D_v) and the root-mean-square strain (ϵ_{RMS}) according to the so-called 'double-Voigt' method⁴⁹ equivalent to the Warren-Averbach approach.⁵⁰ This method, in which Voigt functions were used to describe both the crystallite size and the microstrain contribution to the broadening of the diffraction lines, was performed by using the computer program BREADTH.⁵¹ Physically broadened line profiles (β) were obtained by convolution-fitting approach (program SHADOW⁵²) in which the instrumental profile (diffraction lines of the starting zincite powder) is convoluted with a refinable Voigt function to fit the observed profile (diffraction lines of ball-milled samples). The results of the diffraction line broadening analysis are summarized in Fig. 7.

^{57}Fe Mössbauer spectra were recorded at 20 °C in the transmission mode using a standard *WissEl* (Starnberg, Germany) instrumental configuration. A $^{57}\text{Co}/\text{Rh}$ Mössbauer source was used. The velocity scale and all data refer to the metallic α -Fe absorber at 20 °C. A quantitative analysis of the recorded spectra was made using the *MossWinn* program.

FE SEM/EDS analyses of uncoated samples were made using the field emission scanning electron microscope JSM-7000F (JEOL) equipped with an energy dispersive X-ray spectrometer INCA-350 EDS Microanalysis System (*Oxford Instruments*). In the EDS analysis we used accelerating voltage of 15 kV and probe current of 10 nA. The results of elemental analysis were based on several (at least three) independent EDS measurements performed at low magnification.

Diffuse reflectance UV-Vis-NIR spectra were obtained at 20 °C using a Shimadzu UV-VIS-NIR spectrometer (model UV-3600) equipped with an integrated sphere. Barium sulfate was used as a reference material.

Results and discussion

Color of milling products

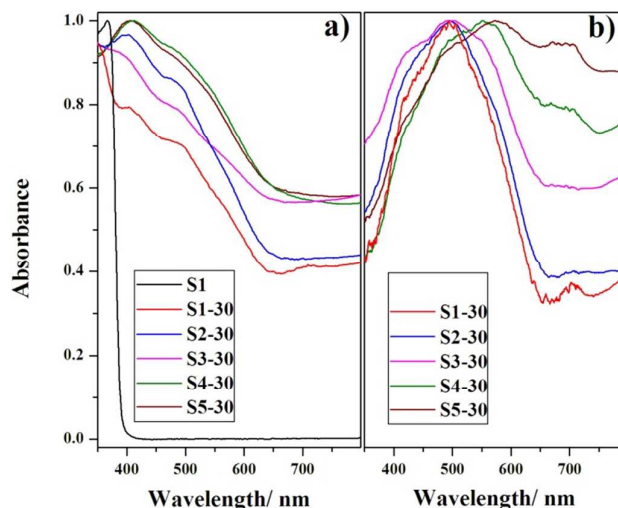


Fig. 1 UV-Vis spectra of pure ZnO (sample S1) and the final milling products (30 h) of samples S1, S2, S3, S4 and S5 (a) and the UV-Vis spectra of samples obtained after calcination of the final milling products at 1000 °C (b).

Similarly as in the case of tempered steel (low chromium content),²⁸ visual examination of products obtained by high-energy milling of pure ZnO (sample S1) with a stainless steel assembly shows that this process has a very strong impact on the chemical and structural properties of milled sample (Section 1 in ESI). The white color of a pure zincite powder changes to white-gray (1 h of milling), greenish gray (5 h of milling), olive (9 h of milling), yellowish brown (14 h of milling) and finally brown (20 h of milling) that remain stable to the impact of further milling up to 30 h and subsequent calcination at 500 and 1000 °C. The color of starting samples S2, S3 and S4 was also white because smaller zincite particles completely covered the surface of bigger iron particles (Section 1 in ESI). However, after only 1 h of milling the color of those samples changed to dark gray (S2-1 and S3-1) and gray (S4-1). After 9 h of milling sample S2 became brown (S2-9) and this color only slightly changed toward red-brown with further milling up to 30 h and subsequent calcination at 500 and 1000 °C. In case of sample S3 a dark brown color appeared after 14 h and slightly changed toward dark red-brown after prolonged milling (30 h). By annealing at 500 and 1000 °C the final milling product (S3-30) lightened and became red-brown. The milling products of samples S4 and S5 changed color in a similar way, from gray to dark gray, almost black, and finally to very dark brown. Calcination at 500 and 1000 °C caused lightening of the final milling products (S4-30 and S5-30), which became red-brown.

The results of UV-Vis diffuse reflectance spectroscopy (Fig. 1) confirm the observed color changes. Starting zinc oxide is transparent in the visible region of the spectrum with a band gap absorption edge at $\sim 390 \text{ nm}$ typical of zincite.⁵³ On the other hand, the product obtained after 30 h of milling (sample S1-30) exhibits, besides the adsorption typical of zincite, absorption in the visible region of the spectrum with a band gap absorption edge at $\sim 650 \text{ nm}$ typical of zinc ferrite.⁵⁴ The spectra of products obtained after

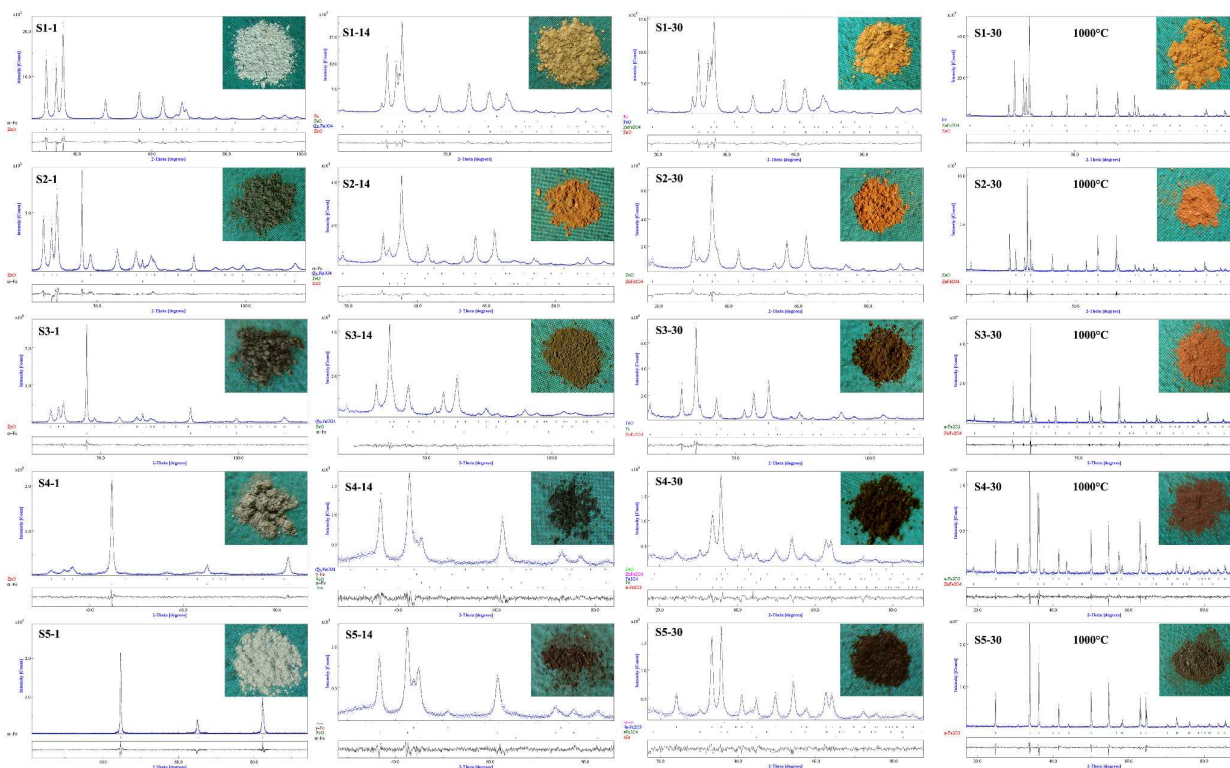


Fig. 2 The results of Rietveld refinements on XRD patterns of the products obtained after ball-milling of the samples S1, S2, S3, S4 and S5 for 1 h, 14 h and 30 h and the products obtained after calcination of the final milling products (30 h) at 1000 °C. Colors of the products are shown in the insets.

30 h of milling samples S2, S3, S4 and S5 show a gradual increase of absorption in the visible region of the spectrum with increased iron content followed by the disappearance of the absorption edge connected with zincite. Calcination of final milling products caused a shift of their absorption maxima toward higher wavenumbers (red shift). Products with a high iron content exhibit high absorption in the whole visible region of the spectrum (dark, almost black color).

Phase analysis

The results of quantitative crystal phase analysis, from the Rietveld refinements of XRD patterns (Fig. 2 and Section 2 in ESI), of the products obtained upon ball-milling of samples S1, S2, S3, S4 and S5 and calcination of the final milling products (30 h) at 500 and 1000 °C are summarized in Fig. 3a and Table 1 in ESI. The XRD pattern of starting zinc oxide (sample S1) contains only the diffraction lines typical of zincite (space group $P6_3mc$, $a = 3.24982 \text{ \AA}$, $c = 5.20661 \text{ \AA}$; ICDD PDF No. 36-1451) (Section 2 in ESI). The ball-milling process caused a significant broadening of these diffraction lines. The first sign of the second crystalline phase, αFe , structurally similar to ferrite ($\alpha\text{-Fe}$, space group $Im\bar{3}m$, $a = 2.8664 \text{ \AA}$; ICDD PDF No. 6-696), appeared after 1 h of milling. Phase W structurally similar to wüstite (FeO , space group $Fm\bar{3}m$, $a = 4.293 \text{ \AA}$; ICDD PDF No. 46-1312) appeared after 5 h of milling and remained present during the whole milling process. Spinel-ferrite phase, phase S , structurally similar to franklinite (ZnFe_2O_4 , space group $Fd\bar{3}m$, $a = 8.433 \text{ \AA}$; ICDD PDF No. 65-3111) appeared after 9 h of milling and significantly

increased upon further ball-milling up to 30 h. Calcination of the final milling product (sample S1-30) at 500 and 1000 °C caused a small increase of phase S followed by the disappearance of phase W and a decrease of phase Z (zincite-type phase) (Fig. 3a).

The XRD patterns of samples S2, S3 and S4 obtained after 1 h of milling contain a mixture of phase αFe and Z with volume ratios in good agreement with the composition calculated for the weight fraction of zinc oxide and iron in the corresponding starting samples (Table 1). The XRD patterns of sample S5 (pure iron) obtained after 1 h of milling contain only the diffraction lines typical of $\alpha\text{-Fe}$. Phase W appeared after 2 h of milling samples S2 through S5 and, unlike sample S1, became the dominant phase after just 5 h of milling. Further milling caused the second onset of transition, which resulted in the appearance and rapid increase of phase S followed by the rapid decrease of phase W . Milling time needed for the onset of $W \rightarrow S$ transition was prolonged with an increase in iron content, from 5 h for sample S2 to 9 h for sample S3 and 14 h for samples S4 and S5. A small amount of the second iron phase, γFe , structurally similar to austenite ($\gamma\text{-Fe}$, space group $Fm\bar{3}m$, $a = 3.6599 \text{ \AA}$; ICDD PDF No. 52-513) appeared in the products of samples S4 and S5 after 9 and 14 h of milling and disappeared upon further milling (Table 1). Prolonged ball-milling of samples S4 and S5 caused the third onset of transition, from phase S to phase H , structurally similar to hematite ($\alpha\text{-Fe}_2\text{O}_3$, space group $R\bar{3}c$, $a = 5.0356 \text{ \AA}$, $c = 13.7489 \text{ \AA}$; ICDD PDF No. 33-664). In the case of

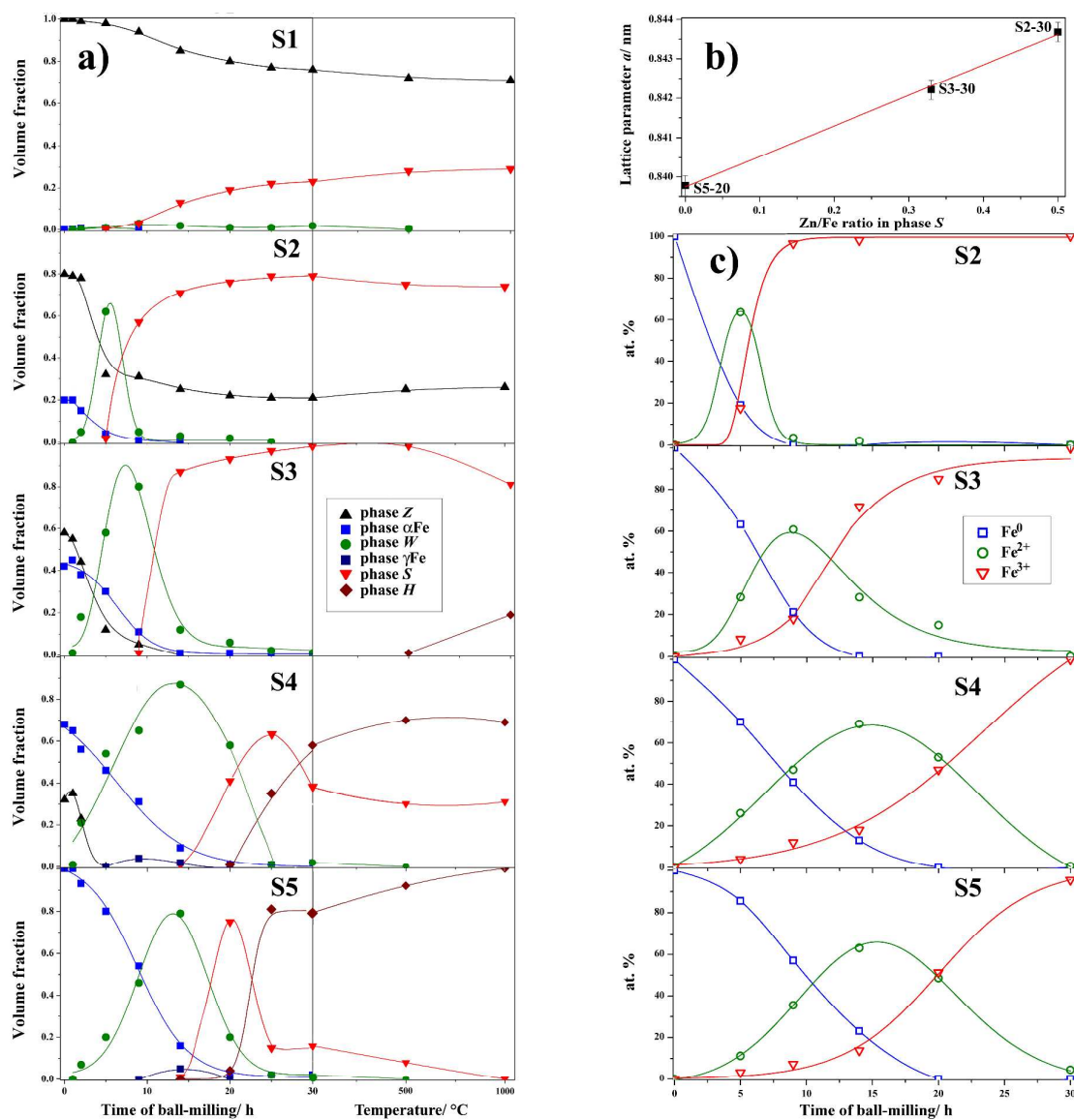


Fig. 3 a) The influence of high-energy ball-milling of the samples S1 to S5 and temperature treatment of the final milling products (30 h) on the crystal phase composition as determined from the results of Rietveld refinements. Phases Z, α Fe, W, γ Fe, S and H are structurally similar to zincite (ZnO), ferrite (α -Fe), wüstite (FeO), austenite (γ -Fe), franklinite (ZnFe_2O_4) or magnetite (Fe_3O_4) and hematite (α - Fe_2O_3), respectively. b) The influence of Zn/Fe ratio in the spinel ferrite lattice (phase S) on the lattice parameter a as determined from the results of Le Bail refinements. c) The iron oxidation states (Fe^0 , Fe^{2+} and Fe^{3+}) in the milled products of the samples S2 to S5 as determined from the results of ^{57}Fe Mössbauer spectroscopy.

sample S5 the onset of $S \rightarrow H$ transition was more pronounced and began earlier (after ~ 20 h of milling) (Fig. 3a).

The lattice parameters of phase S in the products S2-30, S3-30 and S5-20 were determined with precision from the results of Le Bail refinements⁴⁶ of the corresponding XRD patterns with added silicon as an internal standard (Section 3 in ESI). A decrease in parameter a of the spinel-type lattice with the increase in iron content (Fig. 3b) indicates that a franklinite-type lattice, present in products with lower iron content (sample S2-30), shifts with the increase in iron content toward a magnetite-type lattice (Fe_3O_4 , space group $Fd\bar{3}m$,

$a = 8.396 \text{ \AA}$; ICDD PDF No. 19-629), present in the product S5-20. The value of parameter a in the product S3-30 lies between the values obtained in the products S2-30 and S5-20 (Fig. 3b).

Calcination of the final milling products of samples S1 and S2 (samples S1-30 and S2-30) at 500 and 1000 °C has a negligible impact on phase composition. In the case of sample S3-30 calcination caused the appearance (500 °C) and the increase (1000 °C) of phase H. However, phase S remained dominant. Calcination products of samples S4-30 contain a mixture of dominant phase H and a smaller amount of phase S, while in the product of sample S5-30 calcined at 1000 °C a complete $S \rightarrow H$ transition occurred (Fig. 3a).

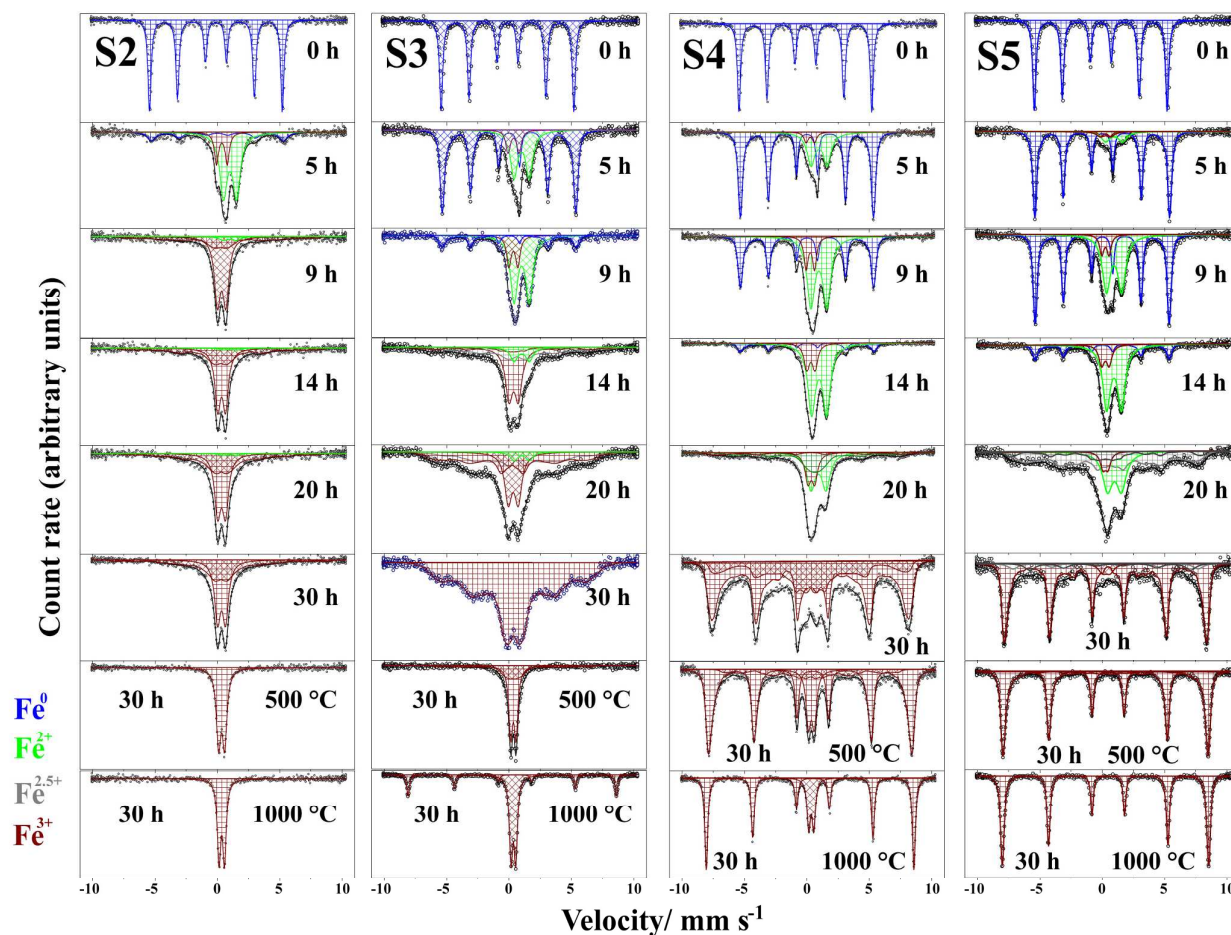


Fig. 4 ^{57}Fe Mössbauer spectra of the starting samples S2, S3, S4 and S5, the corresponding products obtained after 5, 9, 14, 20 and 30 h of ball-milling and the products obtained after calcination of the final milling products (30 h) at 500 °C and 1000 °C.

Mössbauer spectroscopy

The results of ^{57}Fe Mössbauer spectroscopy are summarized in Fig. 4 and Section 4 in ESI. Mössbauer spectra of starting samples S2 to S5 contain only a magnetic sextet with parameters characteristic of $\alpha\text{-Fe}$. Ball-milling caused line broadening in the $\alpha\text{-Fe}$ sextet as a consequence of the widening of hyperfine magnetic field (HMF) distribution due to the crunching of $\alpha\text{-Fe}$ crystals, whereas the intensity (area) gradually decreased and virtually disappeared from the spectra after 9 h (sample S2), 14 h (sample S3) and 20 h (samples S4 and S5) of milling. The early stage of ball-milling caused the appearance and rapid increase of the asymmetric doublet which can be assigned to a defect wüstite (Fe_xO),⁵⁵⁻⁵⁸ in accordance with XRD data (Fig. 3a). Stoichiometric wüstite FeO is not stable at normal atmospheric conditions, thus wüstite always comes in a partially oxidized state.⁵⁹ In the structure of nonstoichiometric wüstite Fe^{3+} ions can be located at octahedral sites (substituting Fe^{2+} ions) or in interstitial tetrahedral sites. The charge is balanced by vacancies in octahedral sites. For that reasons Mössbauer spectra of nonstoichiometric wüstites are very complex and

reported fitting procedures include various numbers of doublets and singlets.^{55-57,60,61}

In the present work, Mössbauer spectra of the products with the highest wüstite content (Fig. 3a) are similar to the spectra of highly oxidized wüstites (Fe_xO , $x \approx 0.9$) reported in the literature.^{55,58,62} Wüstite formed in our products is likely to contain also Zn^{2+} , Ni^{2+} and Cr^{3+} ions, from zincite and the steel impurities, in the Fe^{2+} or Fe^{3+} sites. Reasonably good fits of recorded data were obtained using only two doublets, one for Fe^{2+} and one for Fe^{3+} . The spectra of the samples with high level of zinc were fitted using Fe^{2+} doublet with a distribution of quadrupole splitting (QS) in order to deal with a large number of different environments of Fe^{2+} ions. Isomer shift of Fe^{2+} doublet increased from 0.95 mm s^{-1} in sample S5 to 0.98 mm s^{-1} in sample S4 and to 1.02 mm s^{-1} in sample S3, probably due to incorporation of a significant amount of Zn^{2+} ions into the wüstite structure.

Intensity of Fe^{2+} doublet increased with prolonged ball-milling due to a gradual oxidation of iron from Fe^0 to Fe^{2+} and become dominant after 5 h (sample S2), 9 h (sample S3) or 14 h (samples S4

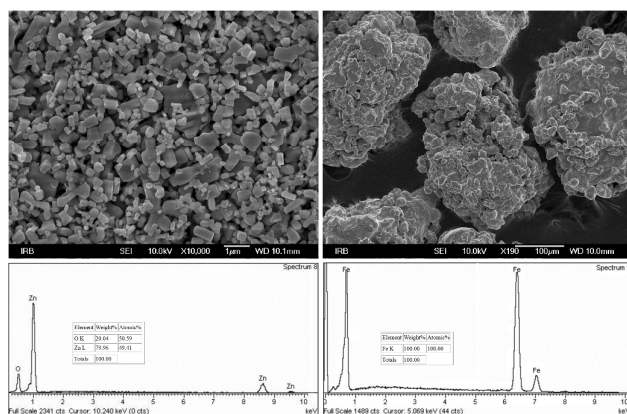


Fig. 5 FE-SEM micrograph of starting zincite (ZnO) (top left) and iron (α -Fe) (top right) powders. The corresponding EDS spectra are shown below. Inset tables show the results of elemental analysis.

and S5) (Fig. 3c). A further ball-milling caused a decrease in intensity of Fe^{2+} doublet and an increase in intensity of Fe^{3+} doublet or broad collapsing sextets. These sextets correspond to partially inverted zinc ferrite (sample S2), to solid solutions between zinc ferrite and magnetite (samples S3 and S4) or to magnetite (sample S5). Mössbauer spectra with collapsing sextets have been commonly recorded for a low crystalline magnetite,^{63,64} as well as for a Zn substituted magnetite.⁶⁵⁻⁶⁷ Finally, after 30 h of ball-milling iron was almost completely oxidised to Fe^{3+} in all samples (Fig. 3c).

In line with the reference literature,⁶⁸⁻⁷⁴ a good fit of Mössbauer spectrum of sample S2-30 was obtained using a doublet and a collapsing sextet with distribution of HMF, which (along with XRD data) indicates the presence of nanostructured partially inverted spinel ZnFe_2O_4 . An increase in QS and overall spectral broadening in Mössbauer spectra of nanostructured zinc ferrite samples is likely to be associated with several factors: increased fractions of disordered and interfacial regions as the grain size decreases, distortions of bond lengths and angles, as well as changes in the distributions of Fe^{3+} and Zn^{2+} ions at octahedral and tetrahedral sites and the appearance of magnetic interactions.^{69,71}

Mössbauer spectrum of the sample S3-30 contains a collapsing sextet with an isomer shift characteristic for Fe^{3+} ($\sim 0.38 \text{ mms}^{-1}$) and a quadrupole shift ($2\epsilon \approx 0.00 \text{ mms}^{-1}$) characteristic for a spinel phase that, in line with the results of XRD analysis, can be represented by a formula $(\text{Fe}^{3+}, \text{Zn}^{2+})_{\text{IV}}[\text{Fe}^{3+}, \text{Zn}^{2+}, \square]_{\text{VI}}\text{O}_4$ (impurities of metal cations from steel contamination are also present in the structure). EDS analysis showed that Fe content is three times higher than Zn, which is manifested as the presence of strong magnetic superexchange interactions between Fe^{3+} ions in tetrahedral and octahedral sites (magnetic sextet in the Mössbauer spectrum). Similar Mössbauer spectrum was recorded on a spinel sample obtained by ball milling of α - Fe_2O_3 and ZnO in the presence of steel impurities.²⁶

Stronger sextet with broad lines, which can be attributed to Zn-hematite, and a weaker collapsing sextet, which can be attributed to Zn-maghemite, are present in the Mössbauer spectrum of the

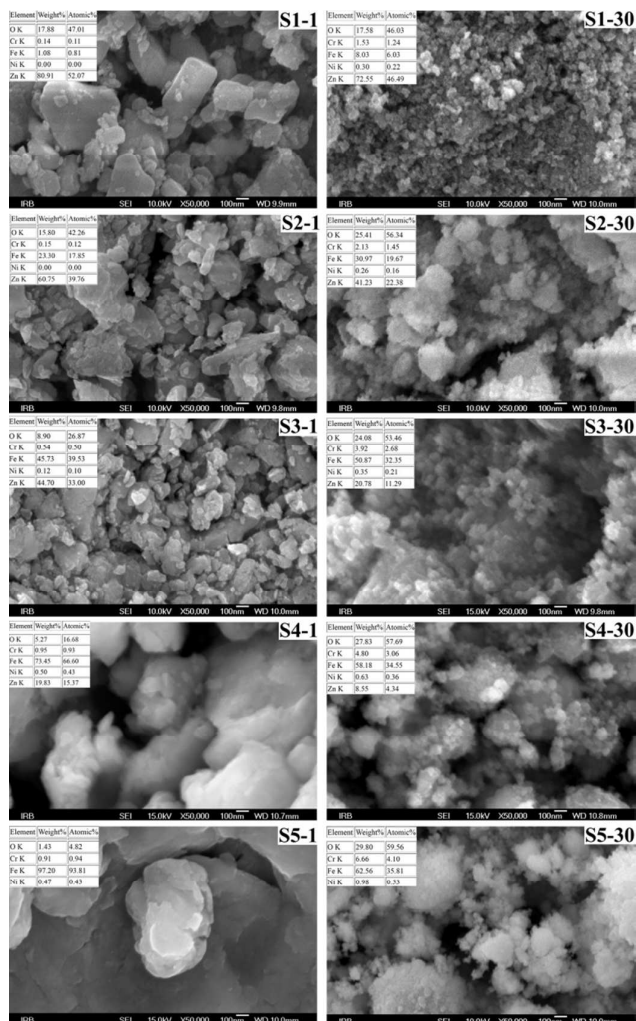


Fig. 6 FE-SEM micrographs at 50 000 \times magnification of the products obtained after 1 h of milling (left) and after 30 h of milling (right). The results of EDS quantitative elemental analysis are given in inset tables (top left).

sample S4-30. These findings are in accordance with the results of XRD analysis (Fig. 3a). Broad sextets of hematite (dominant) and magnetite (minor) are present in the Mössbauer spectrum of the sample S5-30. Line broadening in the spectra is a consequence of very low crystallinity (revealed by FE-SEM and XRD analysis).

Calcination of samples S2-30 and S3-30 resulted with ordering of cations in zinc ferrite from partially inverted toward normal spinel structure (spectrum narrowing). Mössbauer spectra of these samples contain doublet characteristic for the normal spinel ZnFe_2O_4 with only a weak magnetic coupling between Fe^{3+} ions in octahedral positions.^{75,76} The much stronger magnetic interaction between cations in tetrahedral and octahedral positions is not present due to the absence of unpaired electrons in Zn^{2+} ions which occupied all tetrahedral positions.⁷⁷ Calcination of samples S4-30 and S5-30 resulted with transformation of maghemite-type structure to hematite. After calcination at 1000 $^{\circ}\text{C}$ only the most stable phases zinc ferrite (sample S2) and hematite (sample S5), or their mixtures (samples S3 and S4), were present.

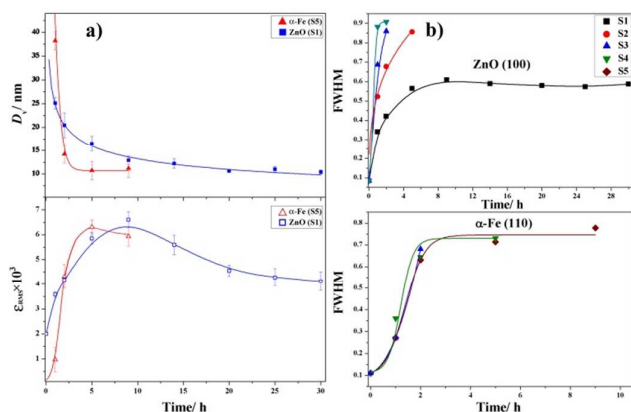


Fig. 7 The influence of ball-milling on the volume-averaged domain size (D_v) and the root mean square strain (ϵ_{RMS}) of ZnO (sample S1) and α -Fe (sample S5) (a) and the full-width at half maximum (FWHM) values of the line 100 of zincite and the line 110 of α -iron in the milling products of all samples (b).

Microstructural analysis

The results of microstructural analysis are summarized in Figs. 5 to 7 and Section 5 in ESI. The FE-SEM micrograph of starting zincite (sample S1-0) shows hexagonal crystals of different shapes and sizes (from ~ 100 nm to ~ 1 μ m) (Fig. 5 left), while the FE-SEM micrograph of starting iron (sample S5-0) contains big particles (>100 μ m) of irregular shape (Fig. 5 right). The process of ball-milling induced a gradual decrease in particle size that in the early stage of ball-milling results in a wide range of sizes and shapes (Fig. 6 left). After prolonged ball-milling all particles (regardless of the ZnO/Fe ratio) decreased to nano dimensions (10 to 20 nm) and became spherical in shape. Significant agglomeration of nanometric particles prevents a clear determination of size distribution (Fig. 6 right and Section 5 in ESI).

The results of line broadening analysis show that the ball-milling of starting zincite (sample S1-0) caused a significant decrease in crystallite size (D_v) and an increase of the micro-strains (ϵ_{RMS}) within the first five hours of milling (Fig. 7a). Lattice micro-strains reached maximum values after ~ 9 h of ball-milling. Further ball-milling up to 14 h causes a small decrease in strain, while crystallite size remains almost unchanged. Further ball-milling up to 30 h has a negligible influence on both the crystallite size and lattice strain in zincite-type products. The first two hours of ball-milling iron (sample S5-0) resulted in an even faster decrease of crystallite size and the increase of lattice microstrains (Fig. 7a). However, the impact of ball-milling rapidly decreased, so the D_v and ϵ_{RMS} values changed very little after ~ 3 h of milling. Due to a significant overlap between the diffraction lines, precise size-strain analyses could not be performed for most of the products obtained by ball-milling samples S2, S3 and S4. However, the obtained full-width at half maximum (FWHM) values of the zincite line 100 indicate higher rate of crystallite size decrease in the presence of iron. On the other hand, the presence of zincite has a negligible impact on the FWHM values of the α -iron line 110 (Fig. 7b).

EDS analysis (Contamination)

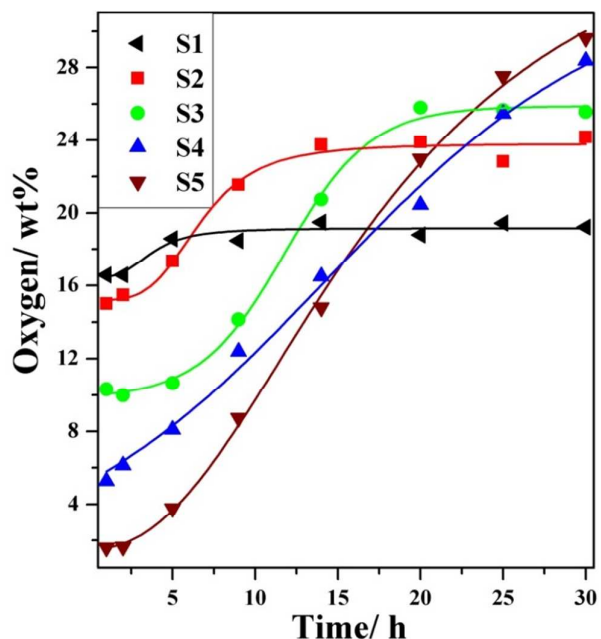


Fig. 8 The influence of high-energy ball-milling on the weight % of oxygen as determined from the results of EDS analysis of the milling products.

Elemental analyses obtained from the EDS results (Section 6 in ESI) show that starting sample S1 contains only elements Zn and O in the atomic ratio 1:1, while starting sample S5 contains only element Fe (Fig. 5 below). Ball-milling of samples caused the appearance of (sample S5) and increase in oxygen content, which becomes more pronounced as the proportion of the starting iron grows (Fig. 8). The increase of oxygen content in samples is the result of the oxidation of iron, present in the initial samples (samples S2, S3, S4 and S5), and steel, introduced due to the wear of milling tools, with the oxygen coming from the milling atmosphere (air).

The presence of iron and chromium contamination is clearly visible after only 1 h of ball-milling of sample S1 (pure zinc oxide) (Fig. 6 and Section 6 in ESI). The amount of those elements increases with the prolonged milling time. The degree of iron contamination in the product of sample S1 obtained after 30 h of milling was similar to that obtained after the corresponding milling of zinc oxide with the balls of tempered steel.²⁸ The EDS spectra of the products obtained after the prolonged milling of samples S1 and S2 also contain a small amount of nickel (Section 6 in ESI). The presence of nickel significantly increases in the products with a higher amount of starting iron (samples S3, S4 and S5). The products of samples S4 and S5 obtained in an earlier milling phase (the first 10 h) contain a relatively high Ni/Cr ratio, which indicates that the contamination of samples mostly came from the vial. However, with the prolonged milling time the Ni/Cr ratio was gradually lowered, so after 30 h of milling the contamination due to the wear of balls was dominant in all the products (Fig. 9 and Section 6 in ESI). The rate of contamination was significantly heightened as the proportion of the starting iron increased (Fig. 9). Weighing of the balls before and after 30 h milling showed a weight loss of 0.39%, 0.65%, 1.53%, 2.25% and 2.44% for samples S1, S2, S3, S4 and S5, respectively.

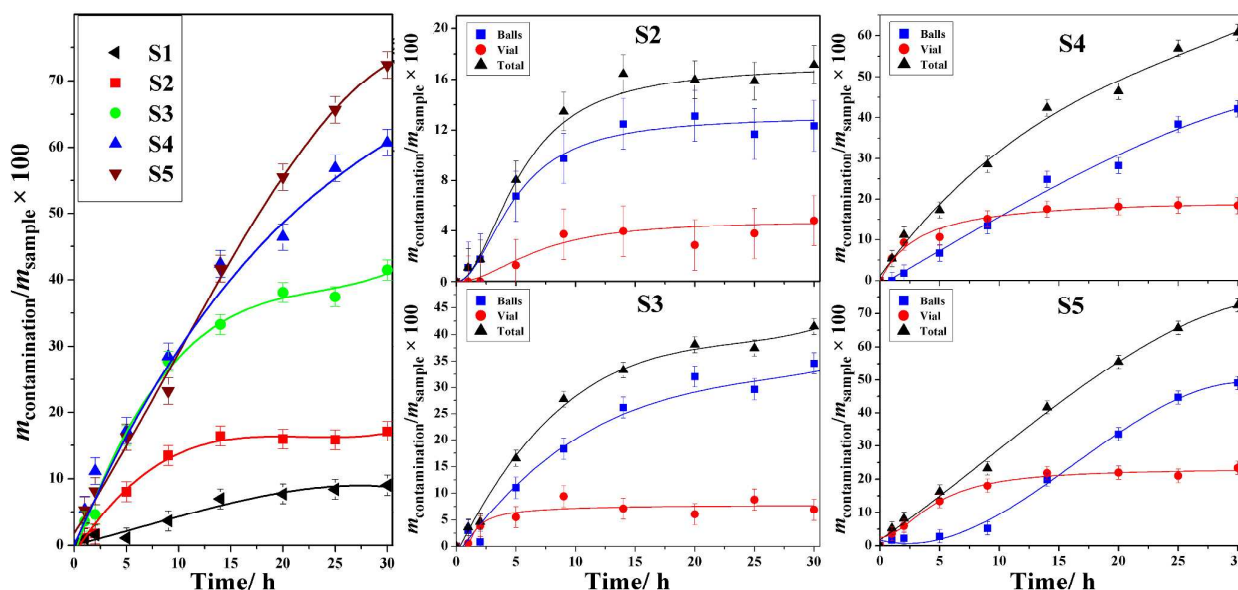


Fig. 9 The influence of high-energy ball-milling of samples S1 to S5 on the amount of steel contamination (left) and the weight ratio of contamination coming from the attrition of balls and the attrition of vial during the high-energy ball-milling of samples S2 and S3 (center) and S4 and S5 (right).

The level of contamination gradually dropped with the prolonged milling time, which can be attributed to the reduction in grain size and the formation of a protective layer on the balls and vial walls. However, this process occurred slowly in the products with a high percentage of starting iron (samples S4 and S5), so the use of “seasoned” milling tools^{8,13} probably would not reduce the level of contamination significantly.

The obtained results show that after 30 h of milling the amount of contamination from the milling tool is about nine times greater in sample S5 (pure iron) than in sample S1 (pure zinc oxide). Such a significant difference in the proportion of contamination cannot be attributed to the difference in hardness between initial samples, which is similar (alpha iron and zinc oxide have hardness between 4 and 5 on the Mohs scale) and significantly smaller compared with hardness of the steel used for milling tools, but to the difference in size and weight of the starting grains. It was shown that the source of contamination (balls or vial) strongly depended on the grain size of milled sample (Figs. 5 and 6). Fine powder of the starting zincite adheres to the wall of the vial and protects it against wear. On the other hand, heavier and coarser grains of iron remain on the bottom of the vial, whereby the side wall remains bare and susceptible to wear due to the impacts with the balls (Fig. 10). As milled grains become smaller they better adhere to the wall of the vial and thereby reduce further contamination due to the wear of the vial. However, a considerable amount of steel particles introduced in the early stage of milling contributes to further wear of the milling tool (mostly balls). Preferred contamination due to the wear of the balls, observed in all samples after prolonged milling, can be attributed to a significantly higher energy released during the frontal collision between two balls moving in the opposite direction compared with the energy released during the collision between the balls and the vial (Fig. 10).

Conclusions

Phase changes caused by ball-milling of samples S1 and S2 can be summarized as follows: $\text{ZnO} + \text{Fe} \rightarrow (\text{Fe,Zn})\text{O} \rightarrow (\text{Zn,Fe})(\text{Fe,Zn})_2\text{O}_4$, whereas $(\text{Fe,Zn})\text{O}$ and $(\text{Zn,Fe})(\text{Fe,Zn})_2\text{O}_4$ stand for solid solutions structurally similar to wüstite and franklinite, respectively. Calcination of the final milling product of these samples had a negligible impact on the phase composition (Fig. 3a). Phase changes caused by ball-milling of samples S3 and S4 were similar but, due to the large quantities of iron, the obtained spinel-ferrite phase appeared to be structurally closer to magnetite. Unlike franklinite, magnetite is metastable and transforms into hematite upon calcination (sample S3) or prolonged milling (sample S4). Phase changes caused by ball-milling of sample S5 can be summarized as follows: $\text{Fe} \rightarrow \text{Fe}_{1-x}\text{O} \rightarrow \text{Fe}_3\text{O}_4 \rightarrow \alpha\text{-Fe}_2\text{O}_3$, whereas Fe_{1-x}O , Fe_3O_4 and $\alpha\text{-Fe}_2\text{O}_3$ stand for phases structurally similar to wüstite, magnetite and hematite, respectively. The results of Mossbauer spectroscopy showed that the observed phase transitions are associated with the oxidation of iron from Fe^0 to Fe^{2+} and from Fe^{2+} to Fe^{3+} .

Although it can be expected that both processes occur simultaneously, the obtained results show that in the earlier period of ball-milling, the duration of which depends on the amount of starting iron, oxidation $\text{Fe}^0 \rightarrow \text{Fe}^{2+}$ dominates. Therefore, after 5 h (sample S2), 9 h (sample S3), and 14 h (samples S4 and S5) of ball-milling a phase structurally similar to wüstite occurs as the dominant, which is accompanied by the dominant presence of iron in the oxidation state of 2+. Further milling resulted in a rapid decrease of the wüstite-type phase and the formation of a spinel-ferrite phase similar to franklinite (ZnFe_2O_4) or magnetite (Fe_3O_4) that is followed by the oxidation of iron from Fe^{2+} to Fe^{3+} .

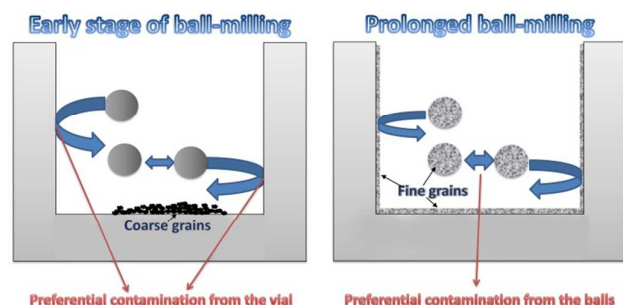


Fig. 10 A schematic illustration of the impact of grain size on the source and the degree of contamination.

The results of our previous studies have shown that the degree of steel contamination during standard high-energy ball-milling is very high and rises significantly if the milling is carried out in the nonoxidative atmosphere of nitrogen (more than three times higher contamination compared with the milling in air atmosphere). In the present study we investigated the effect of size and weight of starting grains on the rate and mechanism of contamination. Ball milling in the oxidative atmosphere of air showed a dramatic increase in the degree of contamination with the increase in the proportion of starting iron (~9 times higher contamination after 30 h of ball-milling of pure iron compared with pure zincite). Significant differences in the amount of contamination were attributed to the difference in size and weight of starting grains. The results of EDS analysis indicated that ball-milling of big and heavy grains (starting iron) caused preferential contamination due to wear of the vial while milling of smaller and lighter grains (obtained upon prolonged milling) caused preferential contamination due to wear of the balls. A significantly higher rate of contamination in the products with higher iron content was attributed to the significant amount of steel chips introduced in the early stages of ball-milling due to wear of the vial, whose abrasive activity promoted further contamination.

Acknowledgements

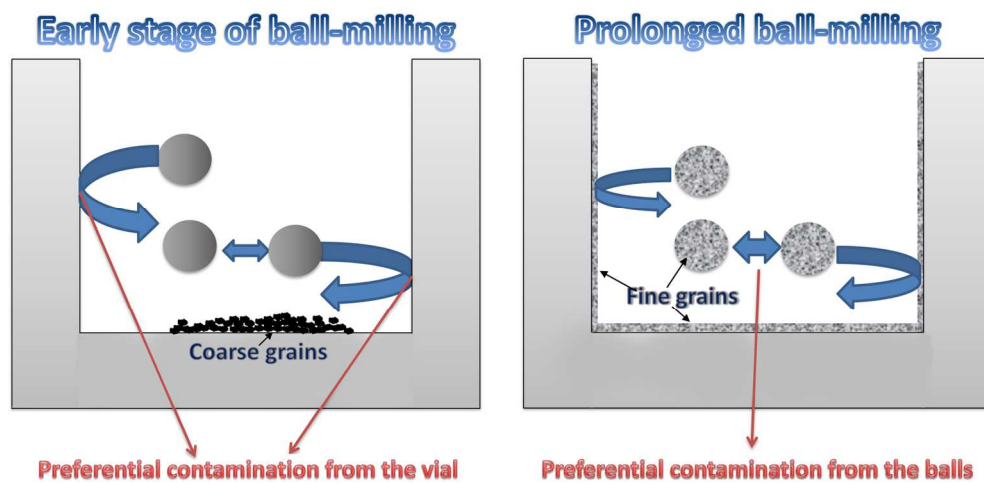
Financial support by the Center of Excellence for Advanced Materials and Sensing Devices, Croatia is gratefully acknowledged.

Notes and references

- 1 S. L. James, C. J. Adams, C. Bolm, D. Braga, P. Collier, T. Friščić, F. Grepioni, K. D. M. Harris, G. Hyett, W. Jones, A. Krebs, J. Mack, L. Maini, A. G. Orpen, I. P. Parkin, W. C. Shearouse, J. W. Steed and D. C. Waddell, *Chem. Soc. Rev.*, 2012, **41**, 413–447.
- 2 T. Friščić, *Chem. Soc. Rev.*, 2012, **41**, 3493–3510.
- 3 L. Takacs, *Chem. Soc. Rev.*, 2013, **42**, 7649–7659.
- 4 T. Friščić, S. L. James, E. V. Boldyreva, C. Bolm, W. Jones, J. Mack, J. W. Steed and K. S. Suslick, *Chem. Commun.*, 2015, **51**, 6248–6256.
- 5 E. Boldyreva, *Chem. Soc. Rev.*, 2013, **42**, 7719–7738.
- 6 B. S. Murty and S. Ranganathan, *Int. Mater. Rev.* 1998, **43**, 101–141.

- 7 C. Suryanarayana, E. Ivanov and V. V. Boldyrev, *Mater. Sci. Eng. A*, 2001, **304–306**, 151–158.
- 8 C. Suryanarayana, *Prog. Mater. Sci.*, 2001, **46**, 1–184.
- 9 V. V. Zyryanov, *Russ. Chem. Rev.*, 2008, **77**, 105–135.
- 10 V. Šepelák, S. Bégin-Colin and G. Le Caërc, *Dalton Trans.*, 2012, **41**, 11927–11948.
- 11 A. F. Fuentes and L. Takacs, *J. Mater. Sci.*, 2013, **48**, 598–611.
- 12 P. Baláž, M. Achimovičová, M. Baláž, P. Billik, Z. Cherkezova-Zheleva, J. M. Criado, F. Delogu, E. Dutková, E. Gaffet, F. J. Gotor, R. Kumar, I. Mitov, T. Rojac, M. Senna, A. Streletskii and K. Wiczorek-Ciurowa, *Chem. Soc. Rev.*, 2013, **42**, 7571–7637.
- 13 C. C. Koch, *Nanostruct. Mater.*, 1997, **9**, 13–22.
- 14 G. Štefanić, S. Musić and A. Gajović, *J. Eur. Ceram. Soc.*, 2007, **27**, 1001–1016.
- 15 G. Štefanić, S. Musić and A. Gajović, *Mater. Res. Bull.*, 2006, **41**, 764–777.
- 16 E. Bailey, D. Lewis, Z. M. Librant, L. J. Porter, *Trans. J. Br. Ceram. Soc.*, **71** (1972) 25–30.
- 17 A. N. Scian, E. F. Aglietti, M. C. Caracocha, P. C. Rivas, A. F. Pasquevich, and A. R. Lopez Garcia, *J. Am. Ceram. Soc.*, 1994, **77**, 1525–1530.
- 18 S. Bid and S. K. Pradhan, *J. Appl. Crystallogr.*, 2002, **35**, 517–525.
- 19 R. C. Garvie, *J. Phys. Chem.*, 1965, **69**, 1238–1243.
- 20 A. Gajović, K. Furić, G. Štefanić, and S. Musić, *J. Mol. Struct.*, 2005, **744–747**, 127–133.
- 21 J. Z. Jiang, F. W. Poulsen, and S. Mørup, *J. Mater. Res.*, 1999, **14**, 1343–1352.
- 22 G. Štefanić, B. Gržeta, K. Nomura, R. Trojko, and S. Musić, *J. Alloys Compd.*, 2001, **327**, 151–160.
- 23 S. Bégin-Colin, G. Le Caërc, M. Zandona, E. Bouzy, and B. Malaman, *J. Alloys Compd.*, 1995, **227**, 157–166.
- 24 T. Kosmac and T. H. Courtney, *J. Mater. Res.*, 1992, **7**, 1519–1525.
- 25 K. Tkáčová, N. Številová, J. Lipka and V. Šepelák, *Powder Technol.*, 1995, **83**, 163–171.
- 26 T. Verdier, V. Nachbaur and M. Jean, *J. Solid State Chem.*, 2005, **178**, 3243–3250.
- 27 F. Padella, C. Alvani, A. La Barbera, G. Ennas, R. Liberatore, and F. Varsano, *Mater. Chem. Phys.*, 2005, **90**, 172–177.
- 28 G. Štefanić, S. Krehula and I. Štefanić, *Chem. Commun.*, 2013, **49**, 9245–9247.
- 29 W. A. Kaczmarek and B. W. Ninham, *IEEE Trans. Magn.*, 1994, **30**, 732–734.
- 30 S. J. Campbell, W. A. Kaczmarek, and G.-M. Wang, *Nanostruct. Mater.*, 1995, **6**, 735–738.
- 31 J. Z. Jiang, Y. X. Zhou, S. Mørup, and C. B. Koch, *Nanostruct. Mater.*, 1996, **7**, 401–410.
- 32 M. Hofmann, S. J. Campbell, and W. A. Kaczmarek, *Mater. Sci. Forum*, 1996, **228–231**, 607–614.
- 33 J. Ding, P. G. McCormick, and R. Street, *Journal of Magnetism and Magnetic Materials*, 1997, **171**, 309–314.
- 34 S. Linderoth, J. Z. Jiang, and S. Mørup, *Mater. Sci. Forum*, 1997, **235–238**, 205–210.
- 35 G. F. Goya, H. R. Rechenberg, and J. Z. Jiang, *J. Appl. Phys.*, 1998, **84**, 1101–1108.
- 36 M. Zdujić, Č. Jovalekić, L. Karanović, M. Mitrić, D. Poletić, and D. Skala, *Mater. Sci. Eng. A*, 1998, **245**, 109–117.
- 37 M. Zdujić, Č. Jovalekić, L. Karanović, and M. Mitrić, *Materials Science and Engineering A*, 1999, **262**, 204–213.
- 38 M. Hofmann, S. J. Campbell, W. A. Kaczmarek, and S. Welzel, *J. Alloys Compd.*, 2003, **348**, 278–284.
- 39 M. Menzel, V. Šepelák and K. D. Becker, *Solid State Ionics*, 2001, **141–142**, 663–669.
- 40 V. Šepelák, M. Menzel, K. D. Becker and F. Krumeich, *J. Phys. Chem. B*, 2002, **106**, 6672–6678.

- 41 T. Verdier, V. Nivoix, M. Jean and B. Hanoyer, *J. Mater. Sci.*, 2004, **39**, 5151-5154.
- 42 C. Alvani, G. Ennas, A. La Barbera, G. Marongiu, F. Padella, and F. Varsano, *International Journal of Hydrogen Energy*, 2005, **30**, 1407-1411.
- 43 V. Šepelák, *Ann. Chim. Sci. Mat.*, 2002, **27**, 61-76.
- 44 H. M. Rietveld, *J. Appl. Cryst.*, 1969, **2**, 65-71.
- 45 L. Lutterotti, S. Matthies and H.-R. Wenk, MAUD (Material Analysis Using Diffraction): A User Friendly Java Program for Rietveld Texture Analysis and More, in: *Proceeding of the Twelfth International Conference on Textures of Materials (ICOTOM-12)*, vol. 1, 1999, p. 1599.
- 46 A. Le Bail, H. Duroy and J.L. Fourquet, *Mater. Res. Bull.*, 1988, **23**, 447-452.
- 47 A. C. Larson and R. B. Von Dreele, *General Structure Analysis System GSAS*, Los Alamos National Laboratory Report, 2001.
- 48 B. H. Toby, *J. Appl. Cryst.*, 2001, **34**, 210-213.
- 49 D. Balzar and H. Ledbetter, *J. Appl. Cryst.*, 1993, **26**, 97-103.
- 50 B. E. Warren, *X-ray Diffraction* (Addison Wesley, Reading, MA, 1969).
- 51 D. Balzar, "BREADTH - a program for analyzing diffraction line broadening", *J. Appl. Cryst.*, 1995, **28**, 244-245.
- 52 S. A. Howard and R. L. Snyder, *Adv. X-ray Anal.*, 1983, **26**, 73-81.
- 53 S. Dutta, S. Chattopadhyay, A. Sarkar, M. Chakrabarti, D. Sanyal and D. Jana, *Progress in Materials Science*, 2009, **54**, 89-136.
- 54 E. Casbeer, V. K. Sharma and X.-Z. Li, *Sep. Purif. Technol.*, 2012, **87**, 1-14.
- 55 N. N. Greenwood and A. T. Howe, *J. Chem. Soc. Dalton Trans.*, 1972, **1**, 110-116.
- 56 C. Gohy, A. Gérard, F. Grandjean, *Phys. Stat. Sol.*, 1982, **74**, 583-591.
- 57 C.A. McCammon, D.C. Price, *Phys. Chem. Minerals*, 1985, **11**, 250-254.
- 58 E. Murad, J.H. Johnston, *Iron Oxides and Oxyhydroxides in: Mössbauer Spectroscopy Applied to Inorganic Chemistry*, vol. 2, edited by G.J. Long, Plenum Publishing Corporation 1987, p. 507.
- 59 R.M. Hazen, R. Jeanloz, *Rev. Geophys. Space Phys.* 1984, **22**, 37-46.
- 60 A. Pattek-Janczyk, B. Sepioł, J.C. Grenier, L. Fournès, *Mat. Res. Bull.*, 1986, **21**, 1083-1092.
- 61 L. Aldon, J.-C. Jumas, *Solid State Sci.*, 2012, **14**, 354-361.
- 62 L. H. Moloto, S. S. Manzini, E. D. Dikio, *J. Chem.*, 2013, 837649.
- 63 A. Hartridge, A.K. Bhattacharya, M. Sengupta, C.K. Majumdar, D. Das, S.N. Chintalapudi, *J. Magn. Magn. Mater.*, 1997, **176**, L89-L92.
- 64 A. G. Roca, J. F. Marco, M. del Puerto Morales, C. J. Serna, *J. Phys. Chem. C*, 2007, **111**, 18577-18584.
- 65 A. C. S. Da Costa, I. G. De Souza Junior, M. A. Batista, D. A. Lopes, K. L. Da Silva, J. V. Bellini, A. Paesano Jr., *Hyperfine Interact.*, 2007, **176**, 107-111.
- 66 P. M. Zélis, G. A. Pasquevich, S. J. Stewart, M. B. F. V. Raap, J. Aphsteguy, I. J. Bruvera, C. Laborde, B. Pianciola, S. Jacobo and F. H. Sánchez, *J. Phys. D: Appl. Phys.*, 2013, **46**, 125006.
- 67 J. M. Byrne, V. S. Coker, E. Cespedes, P. L. Wincott, D. J. Vaughan, R. A. D. Patrick, G. van der Laan, E. Arenholz, F. Tuna, M. Bencsik, J. R. Lloyd, N. D. Telling, *Adv. Funct. Mater.*, 2014, **24**, 2518-2529.
- 68 C.N. Chinnasamy, A. Narayanasamy, N. Ponpandian, K. Chattopadhyay, H. Guérault, J.-M. Greneche, *J. Phys.: Condens. Matter*, 2000, **12**, 7795-7805.
- 69 H. Ehrhardt, S.J. Campbell, M. Hofmann, *J. Alloys Comp.* 2002, **339**, 255-260.
- 70 M. Jean, V. Nachbaur, *J. Alloys Comp.*, 2008, **454**, 432-436.
- 71 V. Nachbaur, G. Tauvel, T. Verdier, M. Jean, J. Juraszek, D. Houvet, *J. Alloys Comp.*, 2009, **473**, 303-307.
- 72 B. Antic, M. Perovic, A. Kremenovic, J. Blanusa, V. Spasojevic, P. Vulic, L. Bessais, E.S. Bozin, *J. Phys.: Condens. Matter*, 2013, **25**, 086001.
- 73 J.S. Jiang, X.L. Yang, L. Gao, J. K. Guo, J.Z. Jian, *NanoStruct. Mater.*, 1999, **12**, 143-146.
- 74 T. Verdier, V. Nivoix, M. Jean, B. Hanoyer, *J. Mater. Sci.*, 2004, **39**, 5151-5154.
- 75 W. Schiessl, W. Potzel, H. Karzel, G. M. Kalvius, A. Martin, M. K. Krause, I. Halevy, J. Gal, W. Schäfer, G. Will, M. Hillberg, R. Wäppling, *Phys. Rev. B*, 1996, **53**, 9143-9152.
- 76 W. Potzel, W. Schäfer, G. M. Kalvius, *Hyperfine Interact.*, 2000, **130**, 241-273.
- 77 C. Kittel: *Introduction to solid state physics*, John Wiley & Sons, Inc., 1996, p 459.



The impact of grain size on the source and the degree of contamination
141x71mm (300 x 300 DPI)